High-resolution determination of the stress in individual interconnect lines and the variation due to electromigration

Qing Ma, S. Chiras, D. R. Clarke, and Z. Suo
Materials Department, College of Engineering, University of California, Santa Barbara, California 93106-5050

(Received 12 January 1995; accepted for publication 6 April 1995)

Large tensile stresses usually exist in metallic interconnect lines on silicon substrates as a result of thermal mismatch. When a current is subsequently passed any divergence of atomic flux can create superimposed stress variations along the line. Together, these stresses can significantly influence the growth of voids and therefore affect interconnect reliability. In this work, a high-resolution ($\sim 2\ \mu$m) optical spectroscopy method has been used to measure the localized stresses around passivated aluminum lines on a silicon wafer, both as-fabricated and after electromigration testing. The method is based on the piezospectroscopic properties of silicon, specifically the frequency shift of the Raman line at 520 R cm^{-1}. By focusing a laser beam at points adjacent to the aluminum lines, the Raman signal was excited and collected. The stresses in the aluminum lines can then be derived from the stresses in the silicon using finite element methods. Large variations of stress along an electromigration-tested line were observed and compared to a theoretical model based on differences in effective diffusivities from grain to grain in a polycrystalline interconnect line. © *1995 American Institute of Physics.*

I. INTRODUCTION

One of the difficulties in developing predictive models for the lifetime reliability of interconnect lines in integrated circuits and packaging is that the residual stresses in the lines, due to such factors as thermal mismatch and intrinsic growth stresses, are largely unknown. These stresses provide one of the driving forces for electromigration induced void formation and growth. Furthermore, the rates of these processes are coupled and are not expected to be linear in stress. In principle, the stress can be computed by finite element methods using standard continuum models for elasticity and plasticity. In practice, however, such an approach is limited by a lack of knowledge of the appropriate constitutive relationships. For instance, while the yield stress and work hardening coefficients of bulk aluminum are known, they are not known with any certainty in the thin-film forms typically used in interconnect metallurgy, especially where there is growing evidence of thickness dependent material properties.[1,2] Similarly, the extent of diffusional relaxation of the stresses on cooling after processing, as well as during any thermal cycling, is not known. Further complications arise because the lines, although polycrystalline along their length, generally are only one, or a few, grains in cross section. This introduces elastic and plastic deformation anisotropy effects that are not normally included in standard finite element codes. Also problematic is the form of the coupling between the residual stress in the line and electromigration induced cavitation. There is thus a need to be able to measure interconnect stresses and to do so with high spatial resolution as a means of validating finite element calculations and constitutive relationships. Unfortunately, obtaining information about the local stresses in interconnects is difficult and few techniques are available. For example, by extending the wafer curvature technique,[3,4] originally designed for measuring stresses in uniform films, the average normal stress component in an interconnect line direction can be determined.[5] More sophisticated x-ray-diffraction techniques can also provide measurements for all three stress components in the lines[6,7] but the techniques are not yet well developed and highly specialized equipment is required. Also, a drawback of both techniques is that they measure the average stresses in a large number of nominally identical lines spaced periodically, and hence cannot provide information about stress variations from line to line, nor the stresses *along* an individual line, as might occur due to stress voiding and electromigration.

To measure the localized stresses along the interconnect lines, and provide a basis for subsequent correlation with observed voiding behavior, an alternative method is required. One such approach is described in this work, namely, the determination of the stresses in the interconnect from the stresses induced in the underlying silicon substrate. These latter stresses, which might collectively be termed the "fringing stress field," are the result of the distortions pro-

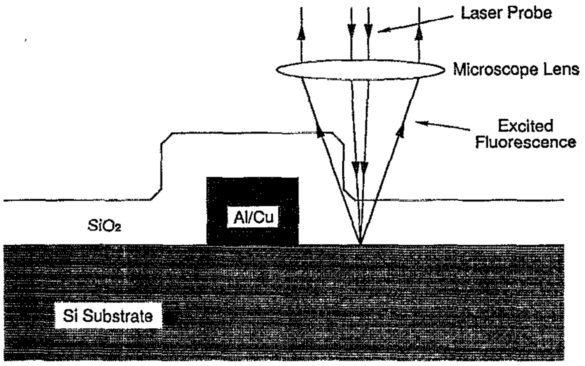

FIG. 1. Schematic illustration of the configurational geometry used in the piezo-spectroscopic measurement of stresses in the vicinity of a passivated interconnect.

duced in the immediate vicinity of the interconnect by the constraint imposed by the substrate and dielectric. They are measurable with relatively high spatial resolution (~2 μm) from the piezo-spectroscopic shift[8,9] in the Raman spectrum excited in the silicon. The stress in the interconnect is then obtained by a self-consistent matching of the measured frequency shift, as a function of distance from an interconnect line, with finite element computations of the stress distribution for the interconnect geometry. The experimental method, described in detail in Sec. IV, consists of measuring the shift in the Raman spectrum obtained in the backscattering geometry using a fine optical probe scanned across the interconnect line, shown schematically in Fig. 1. In our experiments, the wavelength of the laser used to excite the Raman signal was beyond the absorption edge of silicon, thereby precluding making measurements of the silicon directly underneath the interconnects and necessitating measurements in the geometry shown.

In this contribution we describe the basis of the piezo-spectroscopic measurement technique and apply it to determining the residual stress in two as-fabricated interconnects. For illustration, we also present data from an interconnect line after being tested to failure in a standard electromigration test. Prior to presenting the observations, the principal piezo-spectroscopic properties of the silicon Raman spectrum are summarized in Sec. II. Then, in Sec. III, finite element calculations of the stress fields are described together with the calculated stress-induced Raman shifts. The stresses in the interconnects and their differences are the basis for the discussion in Sec. V.

II. PIEZO-SPECTROSCOPIC STRESS MEASUREMENT IN SILICON

The effect of stress on the Raman spectrum of silicon has been described in detail previously[8-10] so only a brief outline of the principal results used in this work are given here. Crystalline silicon is known to have three optical vibration modes, all of which are Raman active. When the propagation direction is along the [001] crystallographic axis, the two transversal modes are along the [100] and [010] directions, respectively, and the one longitudinal mode is along the [001] direction. In the stress-free state, these three modes are degenerate and have a frequency ν_0 at about 520 R cm^{-1}. According to Loudon,[11] the corresponding polarizability tensors are

$$R_1=\begin{pmatrix}0&0&0\\0&0&1\\0&1&0\end{pmatrix},\quad R_2=\begin{pmatrix}0&0&1\\0&0&0\\1&0&0\end{pmatrix},\quad R_3=\begin{pmatrix}0&1&0\\1&0&0\\0&0&0\end{pmatrix}. \tag{1}$$

When the incident illumination and the scattered light are polarized in the direction given by the unit vector $\mathbf{e}_i$ and $\mathbf{e}_s$, respectively, the Raman-scattering efficiency of the mode j is given by the relationship

$$s_j=A|\mathbf{e}_i\cdot R_j\cdot \mathbf{e}_s|^2, \tag{2}$$

where A is a constant. In the particular case of Raman spectroscopy in the backscattering geometry from a (001) surface, it can be verified that only the longitudinal mode R_3 gives rise to a Raman signal.

When silicon is strained, the degeneracy is lifted and the vibration frequencies of the three optical modes shift from ν_0, but by differing amounts according to the nature of the strain tensor. The resulting frequencies can be calculated from the secular matrix equations

$$(\varphi_{ij})=\begin{pmatrix}p\epsilon_{XX}+q(\epsilon_{YY}+\epsilon_{ZZ}) & 2r\epsilon_{XY} & 2r\epsilon_{XZ}\\ 2r\epsilon_{XY} & p\epsilon_{YY}+q(\epsilon_{ZZ}+\epsilon_{XX}) & 2r\epsilon_{YZ}\\ 2r\epsilon_{ZX} & 2r\epsilon_{ZY} & p\epsilon_{ZZ}+q(\epsilon_{XX}+\epsilon_{YY})\end{pmatrix} \tag{3}$$

derived from the dynamic equations with first-order corrections to the spring constants.[8] The strain tensor ϵ_{ij} is defined in the crystallographic coordinates, and p, q, and r are the deformation potential constants, whose values, obtained experimentally,[10] are $p=-1.85\nu_0^2$, $q=-2.31\nu_0^2$, and $r=-0.71\nu_0^2$. The eigenvalues λ_i of this secular equation are related to the strain dependent frequencies by

$$\lambda_i=\nu_i^2-\nu_0^2,\quad i=1,2,3. \tag{4}$$

Since the frequency changes are small this equation may be expanded to give the frequency shift of the Raman mode, i, as

$$\Delta\nu_i=\nu_i-\nu_0\cong\lambda_i/2\nu_0. \tag{5}$$

The Raman polarizability tensors also change with strain and have previously been shown[8] to have the form

$$R_1=\begin{pmatrix}0&0&-1\\0&0&1\\-1&1&0\end{pmatrix},$$

$$R_2=\frac{1}{\sqrt{2+A^2}}\begin{pmatrix}0&A&1\\A&0&1\\1&1&0\end{pmatrix},$$

$$R_3=\frac{1}{\sqrt{2+B^2}}\begin{pmatrix}0&B&1\\B&0&1\\1&1&0\end{pmatrix}, \tag{6}$$

where the parameters A, B, and D are

$$A=(-\varphi_{11}-\varphi_{12}+\varphi_{33}+\sqrt{D})/(2\varphi_{13}),$$

$$B=(-\varphi_{11}-\varphi_{12}+\varphi_{33}-\sqrt{D})/(2\varphi_{13}), \tag{7}$$

and

$$D=(\varphi_{11}+\varphi_{12}-\varphi_{33})^2+8(\varphi_{13})^2. \tag{8}$$

The relative intensity of the two modes contributing to the Raman signal in the backscattering geometry are given by the equations

$$s_2=\frac{1}{N}\frac{A^2}{2+A^2}, \quad s_3=\frac{1}{N}\frac{B^2}{2+B^2}, \tag{9}$$

where N is the normalization parameter

$$N=\frac{A^2}{2+A^2}+\frac{B^2}{2+B^2}. \tag{10}$$

Thus the observed shifts in the Raman spectrum can be related to the elastic strains.

III. FINITE ELEMENT CALCULATIONS

Since the methodology described in this paper for determining the stress in an interconnect line is in essence inferential, detailed calculations of the stress field and the resulting stress-induced shift in the Raman spectrum are necessary. In this section three successive sets of calculation are described. The first is the computation of the stress field in the interconnect and surrounding materials. The second is calculation of the shift in the Raman line as a function of distance from the interconnect line, and the third is the convolution of the stress-induced shift with a finite-sized optical probe.

A series of finite element computations were performed in order to calculate the stress distribution in the underlying silicon substrate produced by the aluminum lines as they cooled from the fabrication temperature. Three different constitutive relations for the deformation behavior of the aluminum lines were assumed. One corresponds to an elastic-perfectly plastic material having a temperature-dependent yield stress.[12,13] The other two correspond to limiting cases, one in which the metal behaves entirely elastically (an infinite yield stress) and the other in which the metal responds hydrostatically (zero yield stress). The latter is of importance since, over time, diffusional relaxation will alter the stress state in an interconnect until it becomes hydrostatic.

The computations were performed for two different linewidths, having the geometry shown in Fig. 2(a), using the ABAQUS code. In the calculations, the normal displacements across all the interfaces were assumed to be continuous so as to represent fully bonded interfaces. The mechanical and the thermal-expansion properties of the silicon substrate and the silica dielectric were those listed in Table I. The effective temperature drop was assumed to be 400 °C, the difference between the processing temperature used in the fabrication of the electromigration lines examined in this work and room temperature.

In the calculations, the stress-free thermal strain of the silicon substrate was taken to be the reference state. That is, the thermal-expansion coefficient of silicon was assumed to be zero, and the thermal-expansion coefficients of the silica and aluminum were correspondingly taken to be $\alpha(\mathrm{SiO_2})-\alpha(\mathrm{Si})$ and $\alpha(\mathrm{Al})-\alpha(\mathrm{Si})$, respectively. As a consequence, the calculations were plane strain.

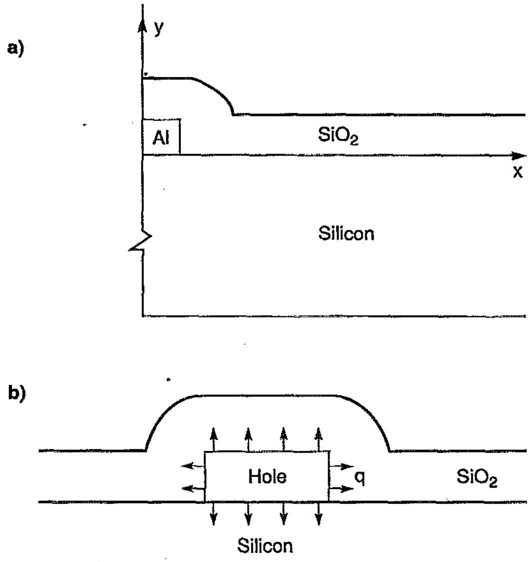

FIG. 2. (a) Two-dimensional geometry used in the finite element computations together with the coordinate system used. (b) The tractions on a hollow interconnect used to model the effect of a hydrostatic stress in an interconnect.

The finite element calculations for the cases in which the aluminum line deformed purely elastically or with an elastic-perfectly plastic response were straightforward. Less straightforward were the calculations for the line deforming in a purely hydrostatic manner. The procedure adopted used the following thought experiment: For the hydrostatic case, the result of all the deformation processes occurring in the line during cooling is to create a hydrostatic stress, denoted as q. Although the general strain history can be complex, the final volume strain is simply the elastic strain plus the thermal-expansion strain, i.e.,

TABLE I. Assumed mechanical properties.

Material	E (GPa)	v	Yield stress (MPa)	$\alpha(10E-6/\mathrm{K})$
Silicon	130	0.28	-	2.3 – 293 K
				2.9 – 373 K
				3.2 – 422 K
				3.4 – 477 K
				3.6 – 533 K
				3.8 – 589 K
				4.0 – 644 K
				4.1 – 723 K
SiO$_2$	94	0.16	-	1.3
Al/Cu	69 @ 293 K	0.33	104 @ 293 K	22.5 @ 293 K
	68 @ 373 K		104 @ 373 K	24.2 @ 373 K
	66 @ 422 K		93 @ 422 K	25.3 @ 422 K
	62 @ 477 K		72 @ 477 K	26.5 @ 477 K
	55 @ 533 K		41 @ 533 K	27.7 @ 533 K
	49 @ 589 K		31 @ 589 K	28.9 @ 589 K
	42 @ 644 K		21 @ 644 K	30.0 @ 644 K
	39 @ 723 K		15 @ 723 K	30.7 @ 723 K

$$\epsilon_x + \epsilon_y + \epsilon_z = Bq - 3\alpha\Delta T, \tag{11}$$

where $B = 3(1-2\nu)/E$ and the materials parameters are for aluminum. To determine q we imagine that the Al line is replaced by a hollow line which is subject to a tensile traction q over its surface [Fig. 2(b)]. In the plane strain problem, the volume strain is the same as the area strain. Let S be the area of the hole and u_n be the normal displacement of the surface. Because both the silica dielectric and the silicon substrate are elastic, the area change of the hollow line must be linear in q and ΔT:

$$\frac{1}{S}\int u_n \, dl = -Cq - D\Delta T, \tag{12}$$

where the integral is over the perimeter l of the hole. Provided the Al line is well bonded the area change produced by the hydrostatic pressure q must be the same for both the Al line and the hole. Thus, by combining Eqs. (11) and (12), the hydrostatic stress is

$$q = \Delta T(3\alpha - D)/(B + C). \tag{13}$$

To calculate the hydrostatic stress, the coefficients C and D are first determined, independently, from the finite element computations for u_n under two separate loading conditions: (i) $q=1$ and $\Delta T=0$ and (ii) $q=0$ and $\Delta T=1$. A comparison of the mean stress in the center point of an interconnect as a function of the temperature drop from the processing temperature for the alternative constitutive behaviors is shown in Fig. 3. In Fig. 3(a) the materials properties are all temperature independent except in the elastic-perfectly plastic case, where the yield stress is temperature dependent. When the full temperature-dependent properties are used, Fig. 3(b), the elastic and elastic-perfectly plastic stresses are greater and are markedly nonlinear with decreasing temperature.

Although the full stress field in the line, dielectric, and the silicon substrate was computed, only the stresses in the center of the line and along the x axis in the silicon substrate are presented here. Since the absorption length in the silicon of the Raman frequency used in the experiments is small (~200 nm), only the stresses calculated in the top row of integration points in the mesh closest to the silicon/silica interface are presented. For purposes of comparison, the stresses in the center of lines and immediately below the line in the silicon are presented in Table II for lines deforming elastically, elastic-perfectly plastically, and hydrostatically. In Fig. 4 the three stress components, σ_{xx}, σ_{xy}, and σ_{yy}, are plotted as a function of distance along the x axis in the silicon for the case in which a 0.8 μm interconnect has deformed in an elastic-perfectly plastic manner.

A feature of the finite element computations is that the hydrostatic stress can be used as a scaling parameter in data fitting. This is rigorously correct for the two limiting cases: the metal behaving elastically and hydrostatically. For cases in between, plasticity theory dictates that after the metal fully yields during cooling, the magnitude of the difference between the largest and smallest stress components in the line is fixed by the metal yield strength,[13,14] rather than being proportional to σ_H. In practice, the real yield stress of the metal alloy is, unfortunately, rarely known, and hence the calculated individual stress components have larger errors than the hydrostatic stress, which depends more weakly on the yield stress. Additional FEM calculations have shown that by changing the value for the yield stress, the variations of the stresses in the substrate on the side of the lines normalized by the hydrostatic stress are found to be insignificant, at least for the two, relatively equiaxed cross-sectional geometries of the interconnects investigated. This suggests that the stress distribution in the substrate will, in the majority of cases, be proportional to the magnitude of the hydrostatic stress.

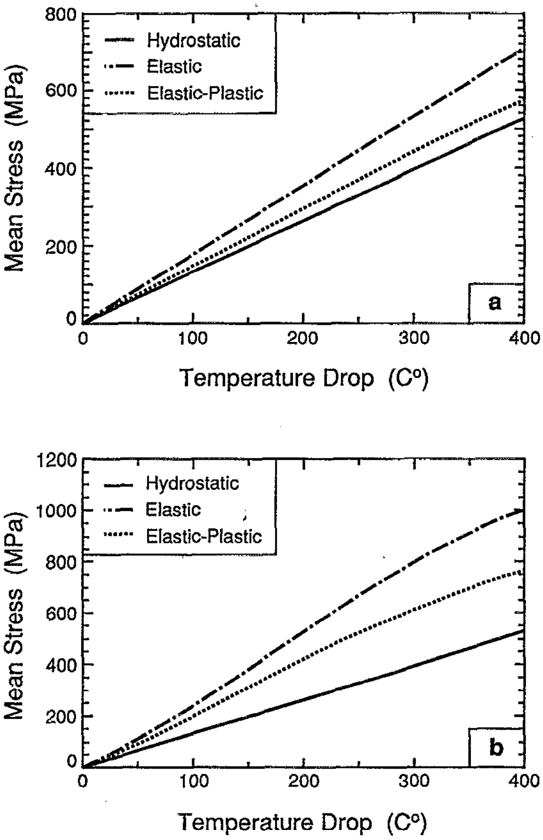

FIG. 3. The thermal-expansion mismatch stress resulting from three alternative constitutive behaviors of a 0.8 μm wide Al–Cu interconnect as a function of cooling from the fabrication temperature, 400 °C. In (a) all the materials properties are temperature independent except for the yield stress in the elastic-perfectly plastic response. In (b) the full temperature dependence of the materials properties are used.

Following the calculation of the stresses in the silicon, the stress-induced Raman shifts as a function of position along the x axis were computed. As mentioned in Sec. II, both vibrational modes 2 and 3 contribute to the backscattering Raman signals when silicon is strained. The frequency shifts for the two modes can be calculated from the secular equation and Eq. (5), using the calculated stresses in Fig. 4, the appropriate coordinates transformation matrix, and the compliance tensor of silicon. The total frequency shift is the average of the two modes weighted by their relative intensities [Eq. (9)]. The stress-induced frequency shifts for the 0.8 μm line are shown in Fig. 5(a), again for an elastic, elastic-perfectly plastic, and hydrostatic deformation of the line.

In practice, in the experiments described below, the stress distribution in the silicon is probed with a focused

TABLE II. Calculated stresses (MPa).

Line center	0.8 μm line Elastic	0.8 μm line Elastic/ plastic	0.8 μm line Hydrostatic	3.0 μm line Elastic	3.0 μm line Elastic/ plastic	3.0 μm line Hydrostatic
σ_{xx}	646	699	531	776	313	208
σ_{yy}	997	788	531	140	200	208
σ_{zz}	1379	814	531	856	292	208
Silicon $x=0$						
σ_{xx}	−467	−222	−108	−164	160	162
σ_{yy}	536	531	532	144	210	208

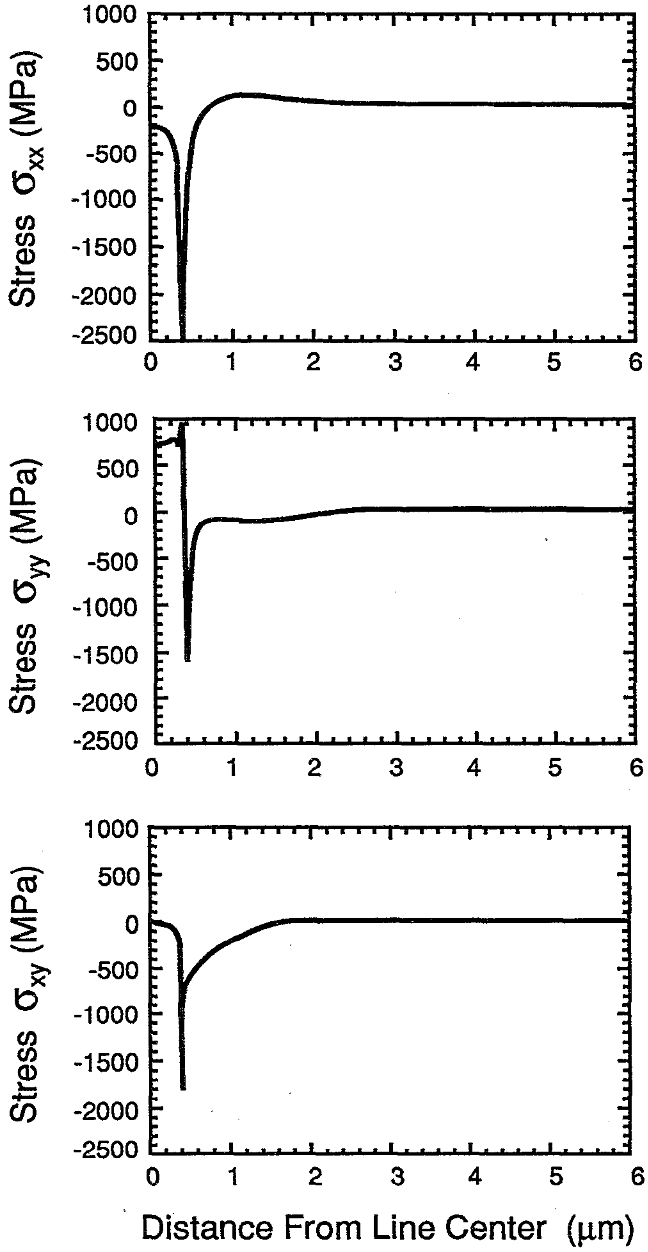

FIG. 4. Calculated stresses in the silicon substrate as a function of the horizontal distance from the center of an 0.8 μm wide interconnect line. The values are taken 0.1 μm below the interface and the line has been assumed to deform in an elastic-perfectly plastic manner.

optical beam. Since the probe sizes used in the Raman experiments are comparable to both the width of the interconnect line and the range of the fringing stress field, the measured frequency shifts as a function of distance can be expected to be a convolution of the actual variation with distance and the finite size of the probe:

$$\overline{\Delta\nu(x)}=\frac{\int_{-x}^{\infty}\Delta\nu(x+u)I(u)du}{\int_{-x}^{\infty}I(u)du}. \tag{14}$$

For the purposes of this work, the intensity profile of the laser probe at its focal plane was assumed to be approximately Gaussian:

$$I(r)=\exp(-2r^2/w^2), \tag{15}$$

where w is the beam width defined in the usual manner at $1/e^2$ of its maximum. For illustration, the convoluted stress-induced Raman shift calculated from the finite element computations for the 0.8 μm line using a Gaussian probe of 1.5 μm is shown in Fig. 5(b).

IV. EXPERIMENTAL METHOD

A. Samples

The interconnect lines investigated were on [001] silicon substrates. They were provided to us from IBM Research and drawn from one of their electromigration test runs. The lines were fabricated by dry etching of 1 μm thickness sputtered films of Al-0.5% Cu deposited (100) wafers. Different width lines ranging from 0.6 to 3 μm were patterned so as to lie along the [110] crystallographic direction of the silicon substrate. A silica passivation layer of ~1 μm thickness was subsequently deposited over the entire substrate by CVD at ~400 °C. Electromigration lifetime tests were conducted on some of the lines until failure, defined as a 20% increase in resistance. All the data obtained during the course of this work was obtained from as-fabricated and electromigration-tested lines on the same chip.

B. Measurement of Raman frequency shift

The stress in the silicon substrate in the vicinity of interconnects was determined from measurements of the piezospectroscopic shifts in the Raman spectra obtained by focusing the laser beam of an optical microprobe onto the region of interest. The measurement configuration is shown schematically in Fig. 1. The procedure adopted was first to iden-

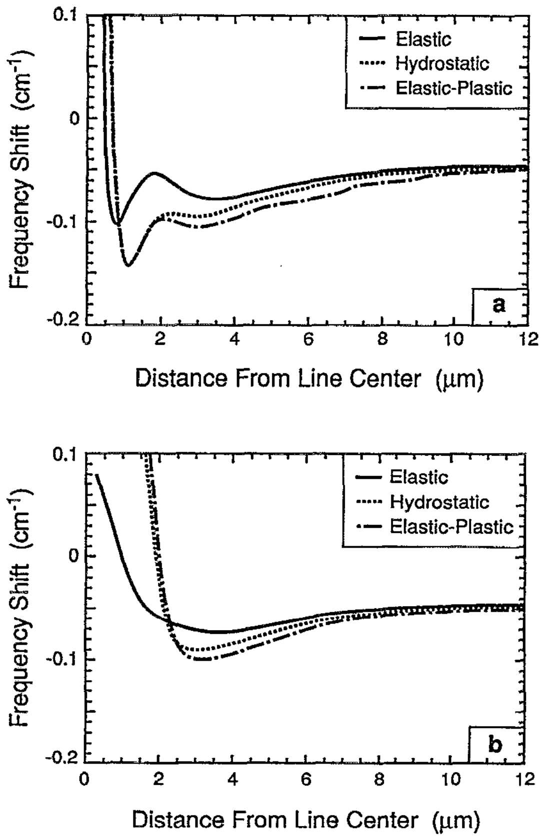

FIG. 5. (a) Computed Raman frequency shift as a function of horizontal distance from the center of the 0.8 μm wide interconnect line. The three curves correspond to the line deforming in an elastic, elastic-perfectly plastic, and hydrostatic manner. (b) The same data but after convoluting with a 1.5 μm Gaussian probe.

tify an interconnect of interest using the optical microscope attached to the microprobe and then obtain a sequence of Raman spectra at successive points on either side of the interconnect line. In each case, the laser was focused at the SiO_2/Si interface and the excited Raman signal collected by the objective lens and guided into the monochromator for frequency analysis. The dispersed spectrum centered around 520 R cm^{-1} was measured using a CCD multichannel detector. The laser used, an argon-ion laser operating at 514 nm, was aligned with its plane of polarization along the [110] direction of the silicon substrate. To avoid local heating from the laser its output intensity was controlled below 20 mW. This value was chosen after a series of experiments were performed at different power levels and the shift in Raman spectrum measured (Fig. 6). To achieve the highest possible spatial resolution and to minimize the optical distortional effects caused by the SiO_2 passivation layer, a 100/1.3 oil immersion microscope lens with an index-matching liquid was used. All the measurements were conducted at room temperature.

When optimally focused, the laser spot size at the SiO_2/Si interface was about 1 μm in diameter. This size was obtained from measurements of the Raman intensity as the probe was placed at successive positions across the edge of a silicon substrate partially masked with a gold film. By operating the probe laser at 514 nm, the absorption depth in the silicon was estimated to be ~200 nm so the majority of the Raman intensity came from within this depth of the SiO_2/Si interface.

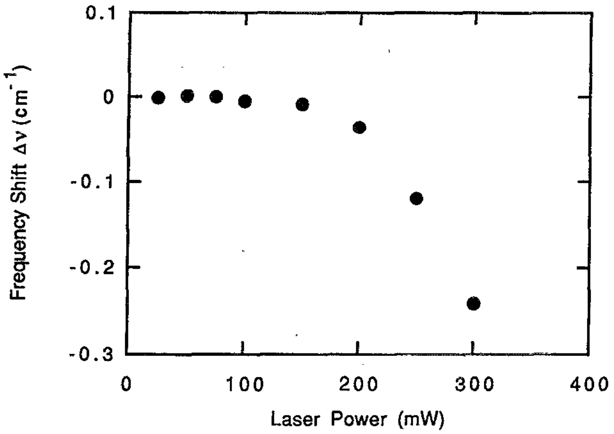

FIG. 6. The dependence of the Raman frequency on the laser power used to form the optical probe.

V. STRESS MEASUREMENTS

A. Residual stress

The residual stress field perpendicular to the as-fabricated interconnect lines was probed first. Figure 7 shows the measured frequency shift distribution perpendicular to one of the 3.0 μm wide lines shown in the upper part of the figure. As expected from the finite element computations, both the stresses and the stress-induced Raman shifts pro-

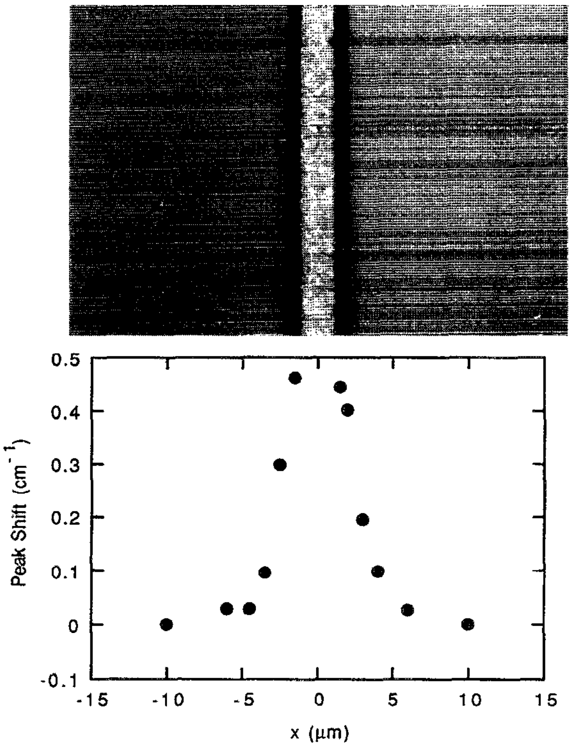

FIG. 7. Measured frequency shift distribution (bottom plot) on the two sides of a 3 μm wide interconnect line (top: optical micrograph).

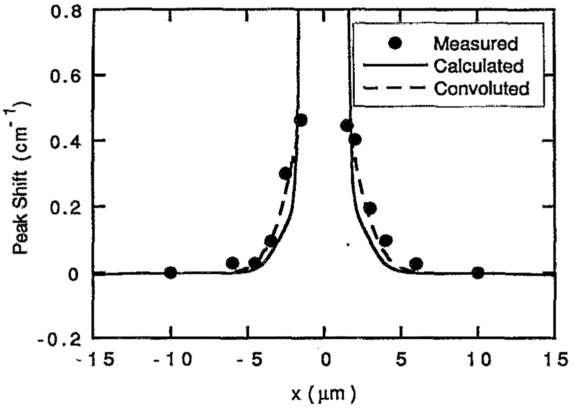

FIG. 8. Comparison between measured and calculated frequency shift for the 3 μm wide interconnect line shown in Fig. 7. The calculated frequency shift distribution is convoluted with the laser beam intensity function.

duced by the line decay rapidly with distance from the line. In Fig. 8 the measured frequency shift is compared with that computed for an elastic-perfectly plastic material (solid line) and after convolution with a 1.5 μm Gaussian probe (dashed line). Although the fit between data and calculations is fairly close, scaling the stress in the interconnect up or down within 15% gave comparable fitting qualities. Therefore, it is concluded that the stress in the metal line is within about 15% of the calculated hydrostatic stress of ~210 MPa.

A similar comparison between the measured frequency shift and the computed frequency profiles are shown in Fig. 9 for one of the 0.8 μm wide interconnects. In this case, after convolution the calculated frequency shift profile for the elastic-plastically deforming interconnect did not adequately fit the measured profile and predicted too large a frequency shift. However, the fit was satisfactory when compared to a purely hydrostatic stress having a value of ~570 MPa, which compares reasonably favorably with the computed hydrostatic stress of 530 MPa (Table II).

B. Electromigration induced stresses

Stress variations along an interconnect can be expected when passing an electrical current through the line if the electromigration atomic flux is not uniform along the line. To investigate such effects, the stresses *along* two 0.8 μm wide lines were measured: one as fabricated, the other after electromigration testing until failure (corresponding to a 20% resistance increase). In making the measurements, the same procedure of measuring the frequency shift perpendicular to the line as described above was used and then measurements were repeated at different points along the interconnect line. By fitting the frequency profiles, the effective hydrostatic stress in the interconnect at the different points was calculated, assuming that the frequency profile is only sensitive to the hydrostatic stress and not particularly sensitive to the deviatoric components.

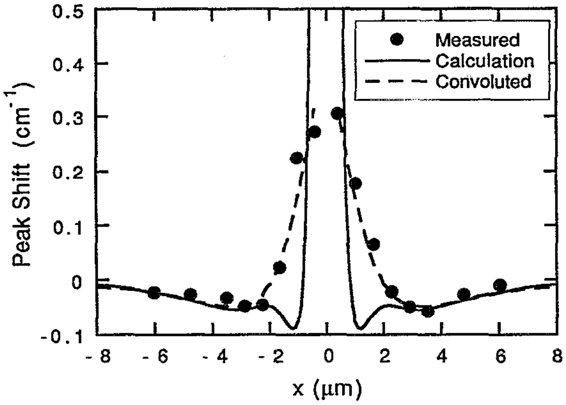

FIG. 9. Comparison between the measured and calculated frequency shift for a 0.8 μm wide interconnect line.

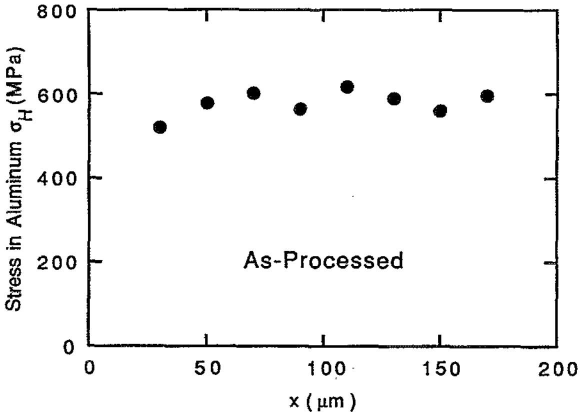

FIG. 10. Hydrostatic stress along the length of an as-fabricated line of 0.8 μm width.

As shown in Fig. 10, for the as-fabricated line, the stresses are, within the experimental error, uniform along the line. The hydrostatic stress in the line is ~570 MPa as determined in the last subsection. If small voids do exist, the stress uniformity along the line suggests that the void distribution is fairly uniform and a small void can only influence the stress state of a very small region around it, and therefore cannot change the stress state in the substrate significantly as expected from St. Venant's principle.

The data for the electromigration tested line is significantly different. As shown in Fig. 11 there are significant stress variations occurring along the length of the line. The variations are much larger than those seen in the as-fabricated adjacent line, indicating that the variations are real and are due to some form of electromigration damage. A second feature of the data is that the overall average stress is also decreased. Third, the stress at each end of the line is approximately the same. Since the hydrostatic stress is expected to be sensitive only to void formation and delamination, the observed decrease in average hydrostatic stress suggests that the electromigration damage is in the form of voiding. (An alternative explanation is presented in the following section.)

VI. DISCUSSION

The comparison of the measured piezo-spectroscopic shift of the Raman spectrum and that computed using alternative constitutive relationships for the deformation behavior

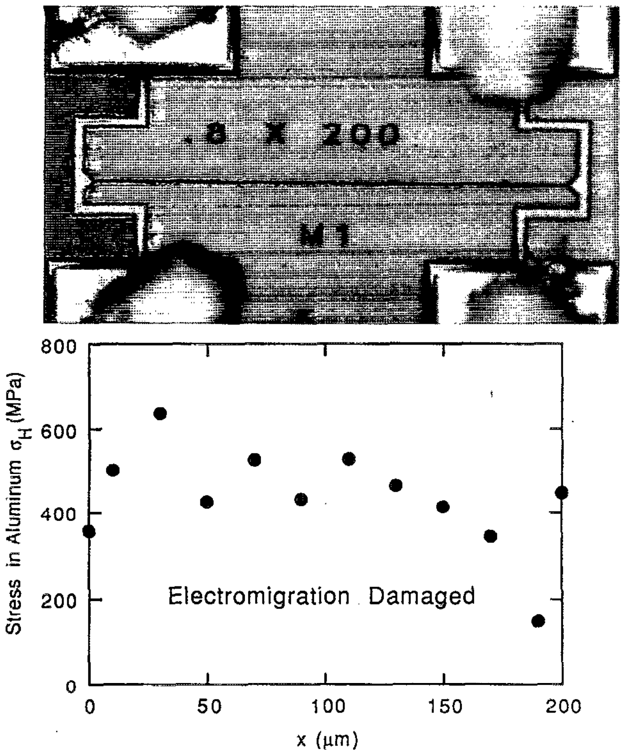

FIG. 11. Hydrostatic stress (bottom plot) along an electromigration-damaged line of 0.8 μm width (top optical micrograph).

of a passivated Al–Cu interconnect suggests that the Raman shift in the adjacent silicon is principally dependent on the hydrostatic stress in the interconnect. While this dependence is not expected to be valid for all metallizations and interconnect cross-sectional geometries, it is of practical utilization for the commonly occurring interconnects, which are usually fabricated out of Al–Cu. The significance of this finding is that it is the hydrostatic stress that provides the drive force for voiding and is also the principal stress component that is altered by electromigration induced material transport. Furthermore, any diffusional and plastic relaxation within an interconnect tends to decrease the deviatoric stresses but leave the hydrostatic stress unaffected.[15] This is expected to be especially so for the micrometer and submicrometer lines presently used in interconnects, since even at room temperature they operate at $\sim 0.3T_m$. When typical Joule heating effects are included, the actual operating temperature of interconnects is closer to $\sim 0.5T_m$. Hence, local measurements of the hydrostatic stress along an interconnect provide a direct indication of changes due to cavitation, or interfacial debonding from the dielectric, or as described below, due to electromigration induced diffusion resulting from diffusional nonuniformities within a polycrystalline interconnect. Complementary experiments, such as void detection by high-voltage SEM[16] or by second- or third-harmonic electrical measurements,[17] are then required to ascertain the microstructural reason for an observed change in hydrostatic stress.

As mentioned above, stress variations, such as those seen in the electromigration-damaged line studied here and presented in Fig. 11, can be due to a number of effects including the existence of relatively large voids. However, it can also occur as a direct result of electromigration in a polycrystalline material irrespective of whether voids are also formed. Figure 7 illustrates a line with an electric current flowing along its length. The line is considered to be divided into a number of segments, each of which has a certain diffusivity. This could be because the film texture along the line changes; e.g., some segments have {111} texture, others are randomly oriented. For the sake of simplicity, assuming interface diffusion dominates, the atomic flux along the interface of segment i is given by[18]

$$J=-\frac{\delta_i D_i}{\Omega kT}Z^*eE+\frac{\delta_i D_i}{kT}\frac{\partial \sigma_i}{\partial x}. \qquad (16)$$

Here the flux J is the flux of atoms that cross a unit length of the interface per second, $\delta_i D_i$ is the interface diffusion parameter, σ_i is the normal stress component at the interface, and other parameters have the usual meanings. At the beginning of the electromigration process, the stress gradient along the line is small, so the flux is controlled by the electrical current. If segment i has a larger diffusivity than the neighboring ones, then material will be accumulated at point A and depleted at point B. A positive stress gradient is then established in segment i. According to Eq. (16), a positive stress gradient will reduce the atomic flux. By the same token, in segments of low diffusivities, the established stress gradient will increase the atomic flux. Therefore, after a transient period, a steady state is established: the atomic flux is constant along the line and the stress state does not change with time. If we assume that (1) the passivation is rigid, (2) the effect of small voids on the stresses can be ignored, and (3) the stress in the line is approximately hydrostatic, then the condition of equal stress at each end of the line imposes

$$\sum_i L_i \frac{\partial \sigma_i}{\partial x}=0. \qquad (17)$$

Combining Eqs. (16) and (17), we have a constant flux along the line given by

$$J=-\frac{(\delta_i D_i)_{\text{eff}}}{\Omega kT}Z^*eE, \qquad (18)$$

where $(\delta_i D_i)_{\text{eff}}$ is the effective average diffusivity along the line defined as

$$(\delta_i D_i)_{\text{eff}}=\frac{\Sigma_i L_i}{\Sigma_i L_i/\delta_i D_i}. \qquad (19)$$

From equation x and y, the stress gradient in segment i can be obtained as

$$\frac{\partial \sigma_i}{\partial x}=\frac{Z^*eE}{\Omega}\left(1-\frac{(\delta_i D_i)_{\text{eff}}}{\delta_i D_i}\right). \qquad (20)$$

Using typical values for the parameter: $Z^*=10$, $e=1.6\times10^{-19}$ C, $\rho=2.5\times10^{-8}$ Ω m, $j=2\times10^{10}$ A m^{-2}, $\Omega=1.6\times10^{-29}$ m^3, and $D_{\text{eff}}/D_i=0.5$, we obtain the stress gradient

$$\frac{\partial \sigma_i}{\partial x}=25 \text{ MPa}.$$

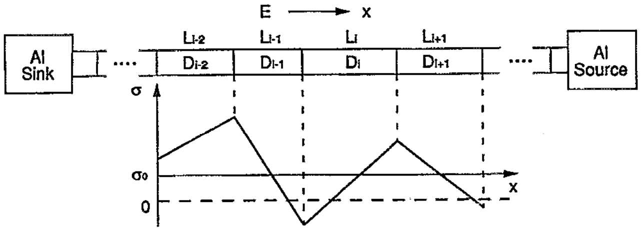

FIG. 12. Illustration of a simple model for the development of stress gradients along an interconnect line due to electromigration. The line is assumed to consist of segments, each of which has a different diffusivity.

Although this is only a rather simple estimate, it is nevertheless of the same order of magnitude as that observed experimentally (Fig. 11).

Finally, it is recognized that more accurate stress measurements could be made directly underneath the interconnect where the stresses are both more uniform and more sensitive to the actual stress level in the interconnect. This is seen in the finite element computations of the stress field, for instance, those reproduced for the 0.8 μm line in Fig. 4. To be able to make such measurements requires the use of Raman spectroscopy at wavelengths at which silicon is transparent. Alternatively, they may be made using a transparent substrate using other microstress measurement techniques. This has recently been achieved by using a transparent substrate incorporating an epitaxial ruby thin-film strain sensor[19] and probing underneath the lines through the substrate.[20]

VII. SUMMARY

Although the stress in an individual interconnect cannot presently be measured with a spatial resolution approaching 1 μm, such spatial resolution is attainable using micro-Raman techniques. We show how this capability can be exploited to probe the stresses, in the underlying silicon substrate, which are generated by the stress in the interconnect and are proportional to them. Finite element computations of the stresses and the stress-induced (piezo-spectroscopic) shift of the Raman lines indicate that the shift in Raman frequency, as a function of distance from an interconnect, is proportional to the hydrostatic stress in the interconnect rather than the deviatoric stresses. This is of particular importance since it is the hydrostatic stress that provides a driving force for stress voiding and electromigration cavitation. Using the methodology developed, micro-Raman measurements recorded in an optical microscope are used to examine the stresses in as-fabricated interconnects and, for illustration, an identical one after electromigration testing. Variations along the length of the electromigration-tested line are noted and attributed to variations in hydrostatic stress.

ACKNOWLEDGMENTS

This work was supported by the Office of Naval Research under Grant No. N00014-J-1875 (Q. M., D. R. C.), by the National Science Foundation through Grant No. MSS-9202165 (Z. S.) and in part by the Parsons Fellowship in Materials (S. C.). The authors are grateful to Dr. M. D. Thouless, now at the University of Michigan, for providing us with the samples used in this work.

[1] W. D. Nix, Metall. Trans. A **20**, 2217 (1989).
[2] A. Bagchi and A. G. Evans, Thin Solids Films (in press).
[3] G. G. Stoney, Proc. R. Soc. London Ser. A **82**, 172 (1909).
[4] P. A. Flinn, in *Thin Films: Stress and Mechanical Properties*, edited by J. C. Bravman, W. D. Nix, D. M. Barnett, and D. A. Smith, MRS Symp. Proc. 130 (Materials Research Society, Pittsburgh, PA, 1989), p. 41.
[5] M. Moske, P. Ho, C. K. Hu, and M. Small, in *Stress-Induced Phenomena in Metallization*, edited by C. Li, P. Totta, and P. Ho (American Institute of Physics, New York, 1992), p. 195.
[6] P. A. Flinn and C. Chiang, J. Appl. Phys. **67**, 2927 (1990).
[7] P. R. Besser, A. S. Mack, D. Fraser, and J. C. Bravman, in *Materials Reliability in Microelectronics III*, edited by K. P. Rodell, W. F. Filter, H. J. Frost, and P. S. Ho, MRS Symp. Proc. 309 (Materials Research Society, Pittsburgh, PA, 1993), p. 287.
[8] E. Anastassakis and E. Burstein, J. Phys. Chem. Solids **32**, 563 (1971).
[9] I. De Wolf, J. Vanhellemont, A. Romano-Rodriguez, H. Norstrom, and H. E. Maes, J. Appl. Phys. **71**, 898 (1992).
[10] E. Anastassakis, A. Cantarero, and M. Cardona, Phys. Rev. B **41**, 7529 (1990).
[11] R. Loudon, Adv. Phys. **13**, 423 (1964).
[12] R. E. Jones, Jr. and M. L. Basehore, Appl. Phys. Lett. **50**, 725 (1987).
[13] A. I. Sauter and W. D. Nix, in *Thin Films: Stresses and Mechanical Properties II*, edited by M. Doerner, W. C. Oliver, G. M. Pharr, and F. R. Brotzen, MRS Symp. Proc. 188 (Materials Research Society, Pittsburgh, PA, 1990), p. 15.
[14] R. Hill, *The Mathematical Theory of Plasticity* (Oxford University Press, New York, 1983).
[15] M. A. Korhonen, C. A. Paszkiet, and C.-Y. Li, J. Appl. Phys. **69**, 8083 (1991).
[16] T. Marieb, J. C. Bravman, P. Flinn, and M. Madden, in *Materials Reliability in Microelectronics IV*, MRS Symp. Proc. 338 (Materials Research Society, Pittsburgh, PA, 1994), p. 409.
[17] Q. Wen and D. R. Clarke (unpublished).
[18] I. A. Blech and C. Herring, Appl. Phys. Lett. **29**, 131 (1976).
[19] Q. Wen, D. R. Clarke, N. Yu, and M. Nastassi, Appl. Phys. Lett. **66**, 293 (1995).
[20] Q. Ma, Q. Wen, and D. R. Clarke, Mater. Res. Soc. Symp. Proc. (in press).